Supplemental Document

OPTICA

General-purpose multi-dimensional parallel optical image processing via liquid crystal superstructures: supplement

Fangtianyu Chen,[1,†] Yiming Wang,[1,†] Dong Zhu,[1] Wen Chen,[1] Sijia Liu,[1] Yiheng Zhang,[1] Rui Sun,[1] Shihui Ding,[1] Lin Zhu,[1] Shijun Ge,[1] Yan-qing Lu,[1,2] and Peng Chen[1,*]

[1] *National Laboratory of Solid State Microstructures, Key Laboratory of Intelligent Optical Sensing and Manipulation, College of Engineering and Applied Sciences, and Collaborative Innovation Center of Advanced Microstructures, Nanjing University, Nanjing 210093, China*

[2] *yqlu@nju.edu.cn*

[†] *These authors contributed equally to this work.*

[*] *chenpeng@nju.edu.cn*

Supplement DOI: https://doi.org/10.6084/m9.figshare.33154184

Parent Article DOI: https://doi.org/10.1364/OPTICA.586957

General-purpose multi-dimensional parallel optical image processing via liquid crystal superstructures: supplement document

FANGTIANYU CHEN,[1,†] YIMING WANG,[1,†] DONG ZHU,[1] WEN CHEN,[1] SIJIA LIU,[1] YIHENG ZHANG,[1] RUI SUN,[1] SHIHUI DING,[1] LIN ZHU,[1] SHIJUN GE,[1] YAN-QING LU,[1,*] AND PENG CHEN[1,*]

[1]*National Laboratory of Solid State Microstructures, Key Laboratory of Intelligent Optical Sensing and Manipulation, College of Engineering and Applied Sciences, and Collaborative Innovation Center of Advanced Microstructures, Nanjing University, Nanjing 210093, China*

[†]*These authors contributed equally to this work.*

**Yan-Qing Lu, yqlu@nju.edu.cn; Peng Chen, chenpeng@nju.edu.cn*

S1. The rationality of phase-only modulation

A. Theoretical derivation

In this section, we explore the impact on PSFs when only the phase component of the standard modulation is employed. The standard modulation has two components: the first is the functional term to implement a specific image processing function. The second term is the grating component that diffracts patterns to target locations. Thus, the modulation H can be simply represented as a superposition of exp(iφ_i) shown in Equation (S1), where φ_i is a complex number that incorporates both the functional term and the grating term.

$$H(f_x, f_y) = \sum_{i=1}^{N} e^{\mathrm{i}\varphi_i} = A(f_x, f_y) e^{\mathrm{i}\Phi(f_x, f_y)}, \tag{S1}$$

A denotes the amplitude of the standard modulation and Φ represents its phase component. We consider a simplified case with only two diffraction patterns, where H= exp(iφ_1) + exp(iφ_2). The corresponding phase can be expressed as

$$e^{\mathrm{i}\Phi} = \frac{H}{A} = \frac{e^{\mathrm{i}\varphi_1} + e^{\mathrm{i}\varphi_2}}{\sqrt{(\cos\varphi_1 + \cos\varphi_2)^2 + (\sin\varphi_1 + \sin\varphi_2)^2}} = \frac{e^{\mathrm{i}\varphi_1} + e^{\mathrm{i}\varphi_2}}{\sqrt{2 + 2\cos(\varphi_1 - \varphi_2)}} \,. \tag{S2}$$

It can be further simplified:

$$\begin{aligned} e^{\mathrm{i}\Phi} &= \frac{e^{\mathrm{i}\varphi_1} + e^{\mathrm{i}\varphi_2}}{\sqrt{2 + 2\cos(\varphi_1 - \varphi_2)}} = \frac{e^{\mathrm{i}\varphi_2}[1 + e^{\mathrm{i}(\varphi_1 - \varphi_2)}]}{\sqrt{4\cos^2\left(\frac{\varphi_1 - \varphi_2}{2}\right)}} \\ &= e^{\mathrm{i}\varphi_2} \frac{[1 + \cos(\varphi_1 - \varphi_2)] + \mathrm{i}\sin(\varphi_1 - \varphi_2)}{2\left|\cos\left(\frac{\varphi_1 - \varphi_2}{2}\right)\right|} = e^{\mathrm{i}\varphi_2} e^{\mathrm{i}\left(\frac{\varphi_1 - \varphi_2}{2}\right)} \frac{\cos\left(\frac{\varphi_1 - \varphi_2}{2}\right)}{\left|\cos\left(\frac{\varphi_1 - \varphi_2}{2}\right)\right|} \end{aligned} \,. \tag{S3}$$

Notice that:

$$e^{\mathrm{i}\left(\frac{\varphi_1 - \varphi_2}{2}\right)} \frac{\cos\left(\frac{\varphi_1 - \varphi_2}{2}\right)}{\left|\cos\left(\frac{\varphi_1 - \varphi_2}{2}\right)\right|} = -\mathrm{i}e^{\mathrm{i}\left(\frac{\varphi_1 - \varphi_2 + \pi}{2}\right)} \frac{\sin\left(\frac{\varphi_1 - \varphi_2 + \pi}{2}\right)}{\left|\sin\left(\frac{\varphi_1 - \varphi_2 + \pi}{2}\right)\right|} = -\mathrm{i}e^{\mathrm{i}\,\mathrm{mod}\left(\frac{\varphi_1 - \varphi_2 + \pi}{2}, \pi\right)} = -\mathrm{i}e^{\frac{1}{2}\mathrm{i}\,\mathrm{mod}(\varphi_1 - \varphi_2 + \pi, 2\pi)} \,. \tag{S4}$$

Here, we introduce a theorem [1] related to complex amplitude modulation, expressed as T(x) = exp(i$M(x)\cdot K(x)$).Both $M(x)$ and $K(x)$ are real valued functions. By utilizing the Fourier-Taylor series expansion, it can be rewritten as

$$T(x) = \sum_{n \in N} T_n(x) e^{\mathrm{i}nK(x)}, \quad T_n(x) = e^{\mathrm{i}[n - M(x)]\pi} \frac{\sin\{[n - M(x)]\pi\}}{[n - M(x)]\pi} \,. \tag{S5}$$

By applying this theorem, Equation (S4) can be expanded using the Fourier series as

$$e^{\frac{1}{2}\mathrm{i}\,\mathrm{mod}(\varphi_1-\varphi_2+\pi,2\pi)} \propto \sum_n e^{\mathrm{i}(n-\frac{1}{2})\pi} \frac{\sin[(n-\frac{1}{2})\pi]}{(n-\frac{1}{2})\pi} e^{\mathrm{i}n(\varphi_1-\varphi_2+\pi)}. \tag{S6}$$

Thus, the phase component of the standard modulation can be expressed as

$$e^{\mathrm{i}\Phi(x,y)} \propto e^{\mathrm{i}(\varphi_2-\frac{\pi}{2})} \sum_n e^{\mathrm{i}(n-\frac{1}{2})\pi} \frac{\sin[(n-\frac{1}{2})\pi]}{(n-\frac{1}{2})\pi} e^{\mathrm{i}n(\varphi_1-\varphi_2+\pi)}. \tag{S7}$$

In Equation (S7), the modulation can be decomposed into infinite series theoretically. We select the two dominant coefficients with the largest absolute values, corresponding to n = 0 and n = 1, yielding results exp(iφ_2) and exp(iφ_1), which precisely correspond to our ideal modulation. While for other high-order diffraction components like n = 3, its intensity is only 1/25 of the target function, exerting minimal impact on the target PSF. Similar trend holds for multiple desired diffraction patterns. As shown in Figure S3(a-d), the phase-only modulation exhibits almost no difference in PSF compared to standard complex modulation, apart from minor higher-order diffraction components, which further validates the rationality of phase-only modulation.

In real practice, we employ digital-micromirror-device to determine the LCs' director orientation distributions. In our numerical simulations, the 2D array representing H consists of 2048×2048 pixels. We extract the central 256×256 region as the effective modulation area and then resize it to 768×768 using the Nearest-Neighbor Interpolation method, which precisely matches the pixel count of digital-micromirror-device.

B. Numerical optimization

In the previous section, we theoretically demonstrated that, compared to standard complex amplitude modulation, phase-only modulation produces extra higher-order diffraction components with low intensity, which are entirely sufficient to achieve the desired PSF. In this section, we employ numerical optimization to validate that the phase component of standard modulation is nearly optimal. The standard modulation can be expressed as the product of intensity and phase as shown in Equation (S1). To prevent light loss and to fully leverage the easy fabrication and geometric phase modulation properties of LCs, we maintain a constant amplitude (A = 1) and confine our optimization to the phase component. The problem is transformed into a mathematical optimization task, whose goal is to determine a phase distribution $\Phi(x, y)$ that minimizes the following loss function [2]:

$$\text{loss} = \left\| h(x,y) - \mathcal{F}\left\{ e^{\mathrm{i}\Phi(x,y)} \right\} \right\|_F^2 . \tag{S8}$$

$\|\cdot\|_F$ denotes the Frobenius norm, $h(x, y)$ represents the desired PSF, with the standard modulation $H(x, y)$ defined as the inverse Fourier transform of h. We employ a gradient descent method based on the PyTorch framework to implement this optimization process, initializing the phase distribution as Φ_0. Take the modulation illustrated in Figure 2 as an example, the desired PSF h_{I} is described in the main text, and its corresponding standard modulation H_1 is shown in Figure S3(a), with the phase component denoted as Φ_1. During the optimization process, we backpropagate gradients and update the weights Φ using the ADAM optimizer for 2000 iterations (with a learning rate of 0.1), and all training was run on an NVIDIA GeForce RTX 4060. Figure S4(a) displays the results for the initialization Φ_0 = constant, while Figure S4(b) presents the outcomes for $\Phi_0 = \Phi_1$; Figure S4(c) illustrates the variation of the loss with iterations for both initializations. It is evident that, regardless of the initial value, the optimization eventually converges to a phase distribution nearly identical to Φ_1. Similar behavior is observed for the other modulations discussed in the main text. It indicates that the phase component of the standard modulation is already very close to the theoretically optimal phase, making it suitable for experimental applications in most cases.

S2. The principle of polarization-encoded parallel image processing based on the spatial translational invariance

In this section, we present a detailed description and derivation of the principle of dual-dimensional parallel processing by NLCs. When LCP light is incident, the output becomes RCP and NLCs impart a geometric phase of 2α. Accordingly, the system's PSF can be approximately expressed as

$$E_{\text{in}} \cdot \left|\mathrm{L}\right\rangle \xrightarrow{\text{NLC}} E_{\text{in}} \otimes \mathcal{F}\left\{e^{\mathrm{i}2\alpha(x,y)}\right\} \cdot \left|\mathrm{R}\right\rangle = E_{\text{in}} \otimes \sum_{i=1}^{N} A_i h_i (x - m_i \Delta x, y - n_i \Delta y) \cdot \left|\mathrm{R}\right\rangle . \quad \text{(S9)}$$

Notably, when RCP light is incident, the geometric phase modulation becomes -2α:

$$E_{\text{in}} \cdot \left|\mathrm{R}\right\rangle \xrightarrow{\text{NLC}} E_{\text{in}} \otimes \mathcal{F}\left\{e^{-\mathrm{i}2\alpha(x,y)}\right\} \cdot \left|\mathrm{L}\right\rangle = E_{\text{in}} \otimes \sum_{i=1}^{N} A_i h_i^* (-x - m_i \Delta x, -y - n_i \Delta y) \cdot \left|\mathrm{L}\right\rangle . \quad \text{(S10)}$$

* denotes the complex conjugate. The spatial coordinates of the i^{th} output are symmetric with respect to the origin, and the corresponding function is the conjugate of the originally odd-symmetric function. Moreover, when E_{in} is input as linearly polarized (LP) light $[1, 0]^{\mathrm{T}}$, it can be regarded as a superposition of equal LCP and RCP components.

$$\begin{aligned} \mathbf{E}_{\text{out}}^{P} &= \sum_{i=1}^{N} A_i E_{\text{in}}(x,y) \otimes \left[h_i(x - m_i\Delta x, y - n_i \Delta y) \cdot |\,\mathrm{R}\rangle + h_i^*(-x - m_i \Delta x, -y - n_i \Delta y) \cdot |\,\mathrm{L}\rangle \right] \\ &= \sum_{i=1}^{N} A_i \left[\xi_i(x,y) \cdot \left|R\right\rangle + \eta_i(x,y) \cdot \left|L\right\rangle \right] \end{aligned} . \quad \text{(S11)}$$

$\xi_i(x, y)$ and $\eta_i(x, y)$ are the outputs of the i^{th} convolution kernels acting on the $\left|R\right\rangle$ and $\left|L\right\rangle$ components, respectively. Here, $\mathbf{E}_{\text{out}}^{P}$ denotes the output optical field, which is originally represented in the basis of orthogonal circular polarization components as shown in Equation (S11). We reformulate it in a more general form using the x-y linear polarization basis.

$$\mathbf{E}_{\text{out}}^{P} = \frac{1}{\sqrt{2}} \sum_{i=1}^{N} A_i \begin{bmatrix} \xi_i(x,y) + \eta_i(x,y) \\ -\mathrm{i}\xi_i(x,y) + \mathrm{i}\eta_i(x,y) \end{bmatrix} . \quad \text{(S12)}$$

It can be observed that the linearly polarized component of the output optical field manifests as a vector superposition of the scalar desired processed function and its center-symmetric conjugate. We present a case with N=2, the two convolution operators (mentioned above) are S(x, y) and 1, assigned to perform two-dimensional edge detection and bright-field imaging, with their spatial coordinates symmetrically positioned at ($-x_0$, 0), (x_0, 0). Especially, the convolution operator kernels S approximately represent mathematical operations $\partial/\partial x + \mathrm{i}\partial/\partial y$ acting on RCP components of output.

$$S(x,y)=\begin{bmatrix}-1+\mathrm{i} & 2\mathrm{i} & 1+\mathrm{i}\\ -2 & 0 & 2\\ -1-\mathrm{i} & -2\mathrm{i} & 1-\mathrm{i}\end{bmatrix}\Rightarrow\frac{\partial}{\partial x}+\mathrm{i}\frac{\partial}{\partial y}, \tag{S13}$$

In contrast, the convolution operator kernels act on LCP components of output is $S^*(-x, -y)$ according to Equation (S10), and its mathematical operations can be expressed as

$$S^*(-x,-y)=\begin{bmatrix}1+\mathrm{i} & 2\mathrm{i} & -1+\mathrm{i}\\ 2 & 0 & -2\\ 1-\mathrm{i} & -2\mathrm{i} & -1-\mathrm{i}\end{bmatrix}\Rightarrow-\frac{\partial}{\partial x}+\mathrm{i}\frac{\partial}{\partial y}. \tag{S14}$$

For brevity, we denote $S^*(-x, -y)$ as S'. Substituting this configuration into Equation (S12), we obtain:

$$\mathbf{E}_{\text{out}}^{P}=\begin{bmatrix}E_{\text{in}}(x-x_0)\otimes S+E_{\text{in}}(x+x_0)\otimes S^{'}\\ -\mathrm{i}E_{\text{in}}(x-x_0)\otimes S+\mathrm{i}E_{\text{in}}(x+x_0)\otimes S^{'}\end{bmatrix}+\begin{bmatrix}E_{\text{in}}(x+x_0)+E_{\text{in}}(x-x_0)\\ -\mathrm{i}E_{\text{in}}(x+x_0)+\mathrm{i}E_{\text{in}}(x-x_0)\end{bmatrix}. \tag{S15}$$

Further simplified, it can be expressed as

$$\mathbf{E}_{\text{out}}^{P}\propto\begin{bmatrix}\frac{\partial}{\partial x}+\mathrm{i}\frac{\partial}{\partial y}+1\\ -\mathrm{i}(\frac{\partial}{\partial x}+\mathrm{i}\frac{\partial}{\partial y}-1)\end{bmatrix}E_{\text{in}}\left(x-x_0\right)+\begin{bmatrix}-\frac{\partial}{\partial x}+\mathrm{i}\frac{\partial}{\partial y}+1\\ \mathrm{i}(-\frac{\partial}{\partial x}+\mathrm{i}\frac{\partial}{\partial y}-1)\end{bmatrix}E_{\text{in}}\left(x+x_0\right). \tag{S16}$$

The output optical field comprises two diffraction patterns, each uniquely encoded with polarization information. We define the diffraction pattern at $(-x_0,0)$ as the +1st order, while that at $(x_0,0)$ corresponds to the -1st order, as illustrated in the schematic diagram Figure S16(c). Taking a circular amplitude and phase object as an example, when LCP light is incident, the +1st order exhibits two-dimensional edge detection, while the -1st order shows bright-field imaging. Conversely, with RCP light as the input, the -1st order yields two-dimensional edge detection, and the +1st order presents bright-field imaging. For an input LP light along the *x*-axis, the output appears as a vector superposition of equal RCP and LCP components. Although both diffraction patterns possess identical intensities, their polarization ellipses exhibit markedly different characteristics. As illustrated in Figure S17(a), (b), the two-dimensional edge significantly enhances the circular arc contours, resulting in very low intensity within the circle. When this effect is superimposed with the bright-field imaging, the central region of the combined optical field retains the polarization state of the bright-field imaging, gradually transitioning to a linear polarization state with increasing radial distance as shown in Figure

S17(c), (d). Furthermore, due to the differing phase distributions in the LCP and RCP components under two-dimensional edges, the polarization angles at the periphery of the two diffraction patterns tend to exhibit nearly opposite trends.

S3. The polarization dimension provides advanced image processing functionalities

In this section, we further demonstrate how to exploit the polarization channel ability to calculate the gradients of an object. As described in the previous section, the diffracted spot is split into two beams. Taking the center of each diffraction pattern as the origin, the two diffraction orders can be expressed as two independent optical fields, as shown in Equation (S17).

$$\mathbf{E}^{1\mathrm{st}} = \begin{bmatrix} \frac{\partial}{\partial x} + \mathrm{i}\frac{\partial}{\partial y} + 1 \\ -\mathrm{i}\left(\frac{\partial}{\partial x} + \mathrm{i}\frac{\partial}{\partial y} - 1\right) \end{bmatrix} E_{\mathrm{in}}, \ \mathbf{E}^{-1\mathrm{st}} = \begin{bmatrix} -\frac{\partial}{\partial x} + \mathrm{i}\frac{\partial}{\partial y} + 1 \\ \mathrm{i}\left(-\frac{\partial}{\partial x} + \mathrm{i}\frac{\partial}{\partial y} - 1\right) \end{bmatrix} E_{\mathrm{in}}\,. \tag{S17}$$

Let $\mathbf{E}^{1\mathrm{st}}$ and $\mathbf{E}^{-1\mathrm{st}}$ denote the optical fields corresponding to the 1^{st} and -1^{st} diffraction orders, respectively. The amplitude of the 1^{st} order diffraction beam measured at an analyzer oriented at angle β can be expressed as

$$\begin{aligned} U^{1st} &= \cos\beta\left(\frac{\partial}{\partial x} + \mathrm{i}\frac{\partial}{\partial y} + 1\right)E_{\mathrm{in}} - \mathrm{i}\sin\beta\left(\frac{\partial}{\partial x} + \mathrm{i}\frac{\partial}{\partial y} - 1\right)E_{\mathrm{in}} \\ &= e^{\mathrm{i}\beta}\left[e^{-2\mathrm{i}\beta}\left(\frac{\partial}{\partial x} + \mathrm{i}\frac{\partial}{\partial y}\right) + 1\right]E_{\mathrm{in}} \end{aligned}\,. \tag{S18}$$

We now focus on the differential term enclosed within the brackets in Equation (S18). By rotating the Cartesian x-y coordinates counterclockwise by 2β (Figure S17(b)), a new m-n system is established in which the factor $e^{-2\mathrm{i}\beta}$ is naturally eliminated:

$$e^{-2\mathrm{i}\beta}\left(\frac{\partial}{\partial x} + \mathrm{i}\frac{\partial}{\partial y}\right)E_{\mathrm{in}} = \left(\frac{\partial}{\partial m} + \mathrm{i}\frac{\partial}{\partial n}\right)E_{\mathrm{in}}\,. \tag{S19}$$

Thus, the complex amplitude of the $+1^{\mathrm{st}}$ diffraction order beam can be simplified as

$$U^{1st}(\beta) = e^{\mathrm{i}\beta}\left(\frac{\partial}{\partial m} + \mathrm{i}\frac{\partial}{\partial n} + 1\right)E_{\mathrm{in}}\,, \tag{S20}$$

Similarly, by repeating the aforementioned steps, the amplitude of the -1^{st} diffraction order can be expressed as

$$U^{-1st}(\beta) = e^{-\mathrm{i}\beta}\left(\frac{\partial}{\partial m} - \mathrm{i}\frac{\partial}{\partial n} - 1\right)E_{\mathrm{in}}\,. \tag{S21}$$

In practical applications, CMOS records only the intensity of diffraction patterns rather than their complex amplitude. Therefore, it is critical to further investigate the intensity distributions of the two diffraction orders. We analyze the cases where the input object is either an amplitude object or a phase object. When the input is an amplitude object, we assume that the phase distributions are uniform, so that the object can be represented as $A(x, y)$. Consequently, the intensity of the +1st diffraction order can be expressed as

$$\begin{aligned} I_{\mathrm{am}}^{1\mathrm{st}}(\beta) &= \left| \left(\frac{\partial}{\partial m} + \mathrm{i}\frac{\partial}{\partial n} + 1 \right) A \right|^2 \\ &= \left| \left(\frac{\partial}{\partial m} + \mathrm{i}\frac{\partial}{\partial n} \right) A \right|^2 + |A|^2 + \left(\frac{\partial}{\partial m} + \mathrm{i}\frac{\partial}{\partial n} \right) A \cdot A^* + \left(\frac{\partial}{\partial m} - \mathrm{i}\frac{\partial}{\partial n} \right) A^* \cdot A \, . \\ &= \left| \left(\frac{\partial}{\partial m} + \mathrm{i}\frac{\partial}{\partial n} \right) A \right|^2 + |A|^2 + 2A \cdot \frac{\partial A}{\partial m} \end{aligned} \tag{S22}$$

the intensity of the -1st diffraction order can be expressed as:

$$I_{am}^{-1st}(\beta) = \left| \left(-\frac{\partial}{\partial m} + \mathrm{i}\frac{\partial}{\partial n} \right) A \right|^2 + |A|^2 - 2A \cdot \frac{\partial A}{\partial m} \, . \tag{S23}$$

It can be observed that the intensity distributions consist of three components: the two-dimensional edges, bright-field imaging and the gradient term. Notably, the gradient terms for the +1st and -1st diffraction orders possess opposite signs, which can be interpreted as the gradient directions differing by π radians.

For a phase object, the amplitude distributions are assumed to be the identity, so the input field can be represented as $A_0 e^{\mathrm{i}\phi(x,y)}$, where A_0 denotes the overall intensity and $\phi(x, y)$ represents the phase distributions. Consequently, the intensity of the +1st diffraction order after analyzer can be expressed as

$$\begin{aligned} I_{\mathrm{phase}}^{1\mathrm{st}}(\beta) &= \left| \left(\frac{\partial}{\partial m} + \mathrm{i}\frac{\partial}{\partial n} + 1 \right) A_0 e^{\mathrm{i}\phi} \right|^2 \\ &= \left| \left(\frac{\partial}{\partial m} + \mathrm{i}\frac{\partial}{\partial n} \right) A_0 e^{\mathrm{i}\phi} \right|^2 + \left| A_0 e^{\mathrm{i}\phi} \right|^2 + \left(\frac{\partial}{\partial m} + \mathrm{i}\frac{\partial}{\partial n} \right) A_0 e^{\mathrm{i}\phi} \cdot A_0 e^{-\mathrm{i}\phi} + \left[\left(\frac{\partial}{\partial m} + \mathrm{i}\frac{\partial}{\partial n} \right) A_0 e^{\mathrm{i}\phi} \right]^* \cdot A_0 e^{\mathrm{i}\phi} \, . \\ &= \left| \left(\frac{\partial}{\partial m} + \mathrm{i}\frac{\partial}{\partial n} \right) A_0 e^{\mathrm{i}\phi} \right|^2 + \left| A_0 e^{\mathrm{i}\phi} \right|^2 - 2A_0^2 \cdot \frac{\partial \phi}{\partial n} \end{aligned}$$

(S24)

the intensity of the -1st diffraction order

$$I_{\mathrm{phase}}^{-1st}(\beta) = \left| \left(-\frac{\partial}{\partial m} + \mathrm{i}\frac{\partial}{\partial n} \right) A_0 e^{\mathrm{i}\phi} \right|^2 + \left| A_0 e^{\mathrm{i}\phi} \right|^2 - 2A_0^2 \frac{\partial \phi}{\partial n} \, . \tag{S25}$$

The output intensity also comprises three components. However, in contrast to the amplitude object input, the gradient terms of the two diffraction orders are completely identical. More importantly, for a given input the first two components remain unchanged, while only the gradient term is determined by the analyzer angle β. This provides significant flexibility for extracting the phase gradients. As shown in Figure S17(c), we record the intensity distributions of the $+1^{st}$ diffraction order under analyzer orientations ranging from 0-165° in steps of 15° for a circular phase pattern input (the yellow double arrows indicate the analyzer angle, while the white arrow indicates the gradient direction). It can be observed that within the same column the upper and lower analyzer orientations differ by 90°, and the gradient directions indicated by the white arrows are exactly opposite. Subtracting these yields the corresponding qualitative phase gradient, as shown in Fig. 5b, with its mathematical expression provided in Equation (9).

S4. Amplitude and phase objects generated by NLC superstructures

NLCs are soft materials that combine the anisotropy of crystals with the fluidity of liquids. They induce a phase retardation between extraordinary and ordinary light due to their inherent birefringence.

$$\Gamma = \frac{2\pi\left(n_{\text{eff}} - n_{\text{o}}\right)d}{\lambda}, \tag{S26}$$

d represents the thickness of the NLC layer, λ denotes the wavelength of the incident light, and n_{o} and n_{eff} correspond to the ordinary and effective extraordinary refractive indices of the NLCs, respectively. Notably, n_{eff} is a function of the LCs' tilt angle θ, which can be electrically controlled. For NLCs characterized by orientation angle α and phase retardation Γ, their modulation effects on vectorial light can be described by the following Jones matrix:

$$\begin{aligned} \mathbf{J} &= \mathbf{R}(-\alpha)\cdot\begin{bmatrix} \exp(-\mathrm{i}\Gamma/2) & 0 \\ 0 & \exp(\mathrm{i}\Gamma/2) \end{bmatrix}\cdot\mathbf{R}(\alpha) \\ &= \cos\frac{\Gamma}{2}\mathbf{I} - \mathrm{i}\sin\frac{\Gamma}{2}\begin{bmatrix} \cos(2\alpha) & \sin(2\alpha) \\ \sin(2\alpha) & -\cos(2\alpha) \end{bmatrix} \end{aligned}, \tag{S27}$$

where $\mathbf{R}$ is the rotation matrix and $\mathbf{I}$ is the identity matrix. In most cases, NLCs are operated under half-wave conditions, $\Gamma = \pi$.

$$\mathbf{J} = \begin{bmatrix} \cos 2\alpha & \sin 2\alpha \\ \sin 2\alpha & -\cos 2\alpha \end{bmatrix}. \tag{S28}$$

With circularly polarized incident light, LCP for $[1, \mathrm{i}]^{\mathrm{T}}$ and RCP for $[1, \text{-i}]^{\mathrm{T}}$:

$$\mathbf{J}\begin{bmatrix} 1 \\ \mathrm{i} \end{bmatrix} = e^{\mathrm{i}2\alpha}\begin{bmatrix} 1 \\ \text{-i} \end{bmatrix}, \quad \mathbf{J}\begin{bmatrix} 1 \\ \text{-i} \end{bmatrix} = e^{-\mathrm{i}2\alpha}\begin{bmatrix} 1 \\ \mathrm{i} \end{bmatrix}. \tag{S29}$$

For LCP incident light, the transmitted light becomes RCP and acquires a geometric phase of 2α; conversely, for RCP incidence, the transmitted light converts to LCP with an opposite phase of -2α (Figure S15(a)). Based on this principle, we can generate an arbitrary phase distribution $2\alpha(x, y)$ by employing a digital micromirror device to set the orientation vector distributions of NLCs to α and then illuminating the NLC with LCP. For example, we map an open-source red blood cell phase image onto the orientation distributions of the NLC, as depicted micrograph of Figure S19(d), which is subsequently used for phase reconstruction experiments (Figure 5).

For the generation of the amplitude object, we illuminate the NLC with a LP beam $[1, 0]^{\mathrm{T}}$

and then analyze the transmitted light oriented along the y-axis. Consequently, the output light field is given by:

$$\mathbf{E}_{\mathrm{out}}=\begin{bmatrix}0&0\\0&1\end{bmatrix}\begin{bmatrix}\cos 2\alpha & \sin 2\alpha\\ \sin 2\alpha & -\cos 2\alpha\end{bmatrix}\begin{bmatrix}1\\0\end{bmatrix}=\sin 2\alpha\begin{bmatrix}0\\1\end{bmatrix}. \tag{S30}$$

Therefore, for any normalized intensity distribution $I(x,\ \mathrm{y})$, it is sufficient to ensure that the orientation distribution of the NLCs satisfies:

$$\alpha=\frac{1}{2}\arcsin\sqrt{I(x,y)}\,. \tag{S31}$$

As shown in Figure S19(a–c), the micrographs display intensity masks generated by NLCs, corresponding to a superimposed square–diamond pattern, a regular octagon, and a circular mask, respectively.

S5. Differential phase-contrast imaging based on phase gradients

In our dual-dimensional image processing framework, the polarization channel not only provides calculating omnidirectional gradients but also demonstrates significant potential in wavefront sensing and bio-imaging. Fundamentally, this approach aims at the retrieval of the wavefront profile $\phi(x, y)$. The employed technique differential phase-contrast (DPC) imaging [3,4], reconstructs the phase distribution of an input phase object by acquiring its gradients. As illustrated in Figure S20, the proposed DPC imaging workflow is structured within our dual-dimensional image processing system, which is based on NLC superstructures in a 4f optical configuration. The phase sample propagates through this system and split into two beams with specific polarization characteristics.

To extract the gradients, we record the 1st order diffraction patterns under four analyzer orientations: 0°, 45°, 90°, and 135°, yielding intensity measurements I_1, I_2, I_3 and I_4. The phase gradients along the y-direction $\nabla_y\phi$ is obtained from $I_1 - I_3$, while the x-direction gradients $\nabla_x\phi$ is derived from $I_2 - I_4$. With these x- and y-orientation phase gradients, we define a complex field g(x, y) as

$$g(x,y) = \frac{\partial\phi(x,y)}{\partial x} + \mathrm{i}\frac{\partial\phi(x,y)}{\partial y}. \tag{S32}$$

Then, its Fourier transform can be written as

$$\mathcal{F}\{g(x,y)\}_{k_x,k_y} = \int_{-\infty}^{+\infty}\int_{-\infty}^{+\infty} g(x,y)\cdot e^{-2\pi\mathrm{i}(k_x\cdot x+k_y\cdot y)}\,dxdy = 2\pi\mathrm{i}(k_x+\mathrm{i}k_y)\cdot\mathcal{F}\{\phi(x,y)\}_{k_x,k_y}. \tag{S33}$$

(k_x, k_y) represents the reciprocal space coordinates corresponding to (x, y). The wave front profile $\phi(x, y)$ can be obtained by inverse Fourier transform Equation (S34), yielding [5]

$$\phi(x,y) = \mathcal{F}^{-1}\left\{\frac{\mathcal{F}\{\nabla_x\phi(x,y)+\mathrm{i}\nabla_y\phi(x,y)\}_{k_x,k_y}}{2\pi\mathrm{i}(k_x+\mathrm{i}k_y)}\right\}. \tag{S34}$$

In principle, $\phi(x, y)$ can be acquired through a straightforward one-dimensional integration. However, in practice, such integration frequently leads to phase images that exhibit undesirable artifacts. By employing phase gradients along two orthogonal directions, the method effectively mitigates the noise issues in DPC images. Furthermore, this approach yields reliable phase reconstructions even when linear integration is impractical, such as in the presence of phase wrapping or imaging large objects.

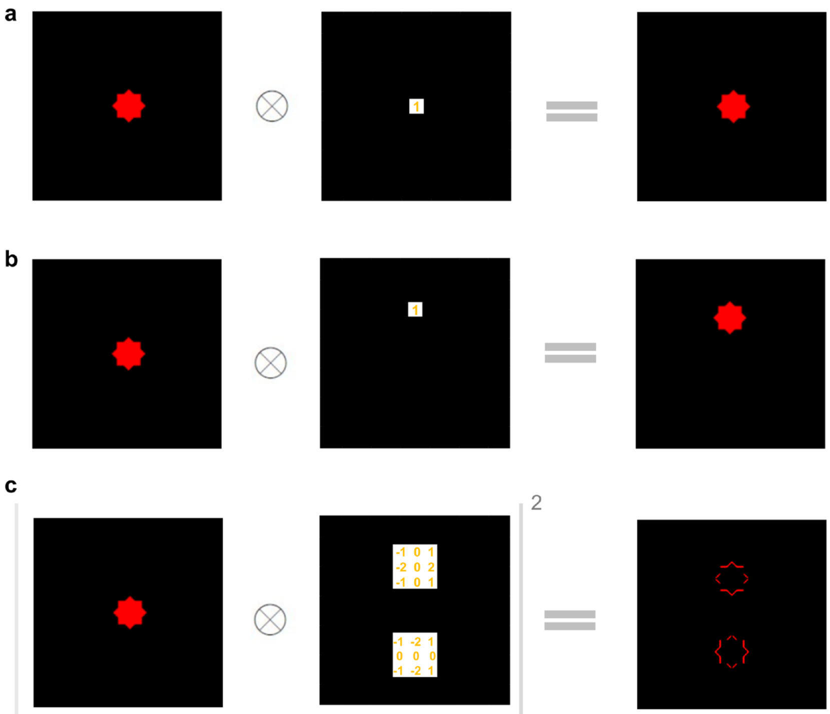

Fig. S1. Translational invariance of convolution operators. (a) The convolution kernel is an identity kernel, resulting in an output identical to the input. (b) The kernel is shifted upwards, and the output also shifts upwards accordingly, demonstrating translational invariance. (c) Horizontal and vertical edge detection kernels are used to detect edges in the x and y directions simultaneously.

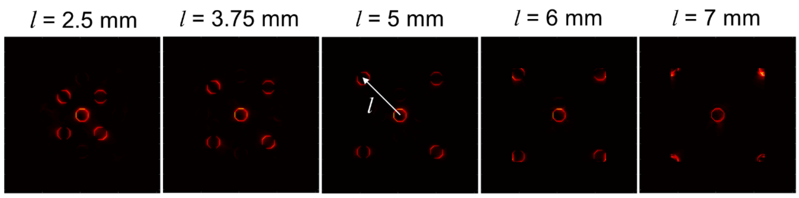

Fig. S2. Influence of the shift distance l on the performance of parallel image processing within and outside the paraxial boundary.

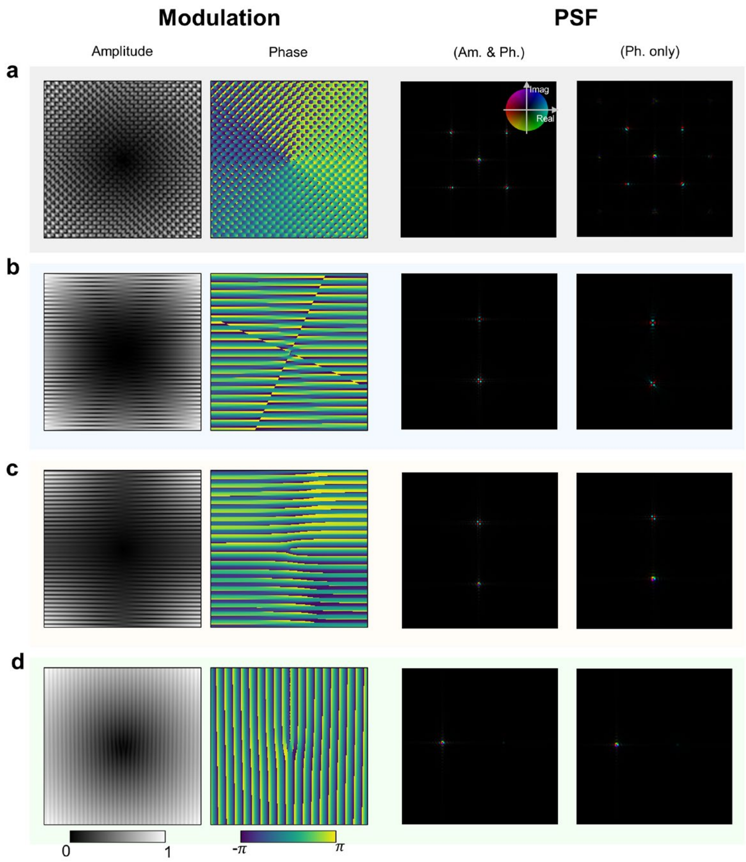

Fig. S3. PSFs of the 4f system under different modulations. This figure illustrates the differences of the system's PSF between complex amplitude modulation and pure phase modulation. The first and second columns represent intensity modulation and phase modulation, respectively, while the third and fourth columns show the system's PSF under complex amplitude modulation and pure phase modulation. The hue in the HSV color space indicates the phase of the PSF, while the value represents its intensity. (a)–(d) correspond to the modulations employed in Fig. 2, Fig. 3(b), Fig. 3(d), and Fig. (4) of the main text, respectively.

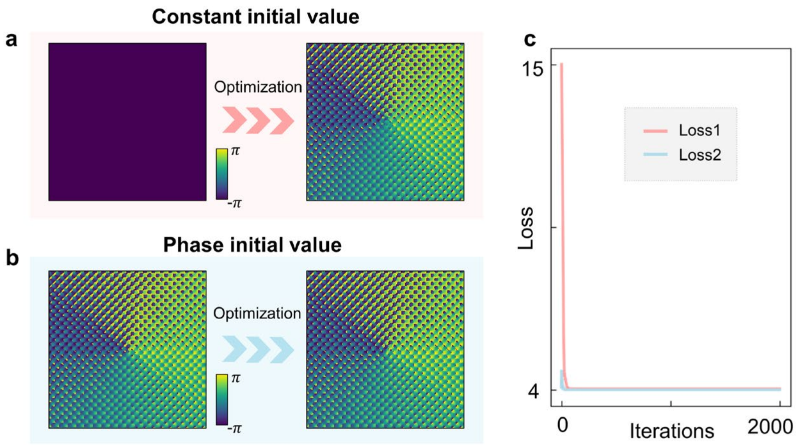

Fig. S4. Phase optimization under different initial conditions. (a) shows the optimization result with a uniform initial phase distribution, while panel (b) presents the outcome when the initial value is set to the phase component of the standard complex amplitude. (c) demonstrates the evolution of the loss function values as a function of iterations for both initial conditions.

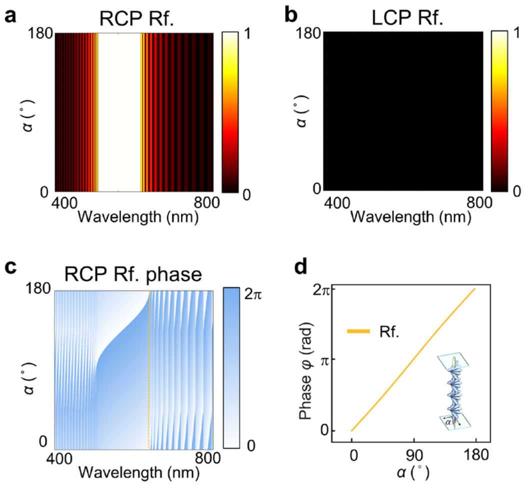

Fig. S5. Spin-selective PBG and geometric phase of right-handed CLC. (a), (b) Simulated reflection for RCP (a) and LCP (b) incident light at different wavelengths and orientation angles. (c) Simulated geometric phase for reflected RCP light at different wavelengths and CLCs' orientation angles α. The color bars indicate the value of phase. (d) Geometric phase of CLC, the relationship between phase and orientation angle: $\varphi = 2\alpha$; Inset: right-handed CLC nanostructure.

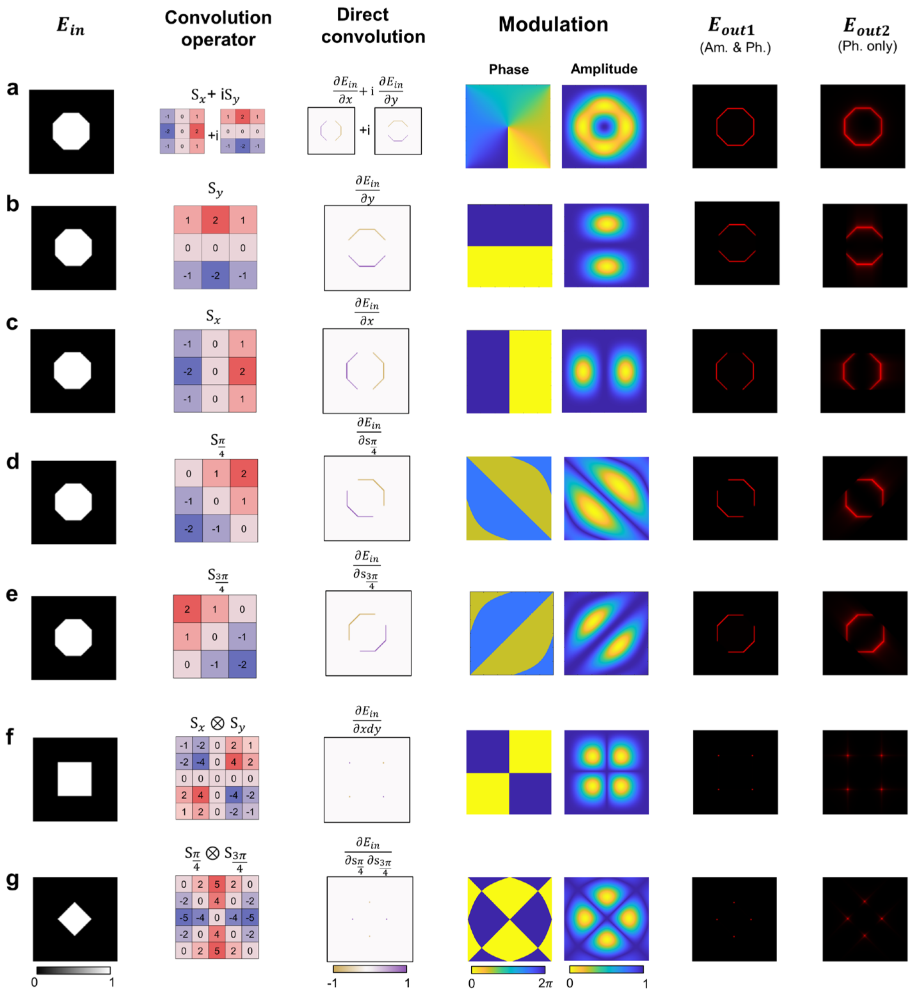

Fig. S6. Versatile convolution operators. This figure illustrates the application of various convolution operators on an input field E_{in} and their corresponding modulation effects. Each row represents a different convolution operator, showing the direct convolution results and the corresponding modulation at Fourier plane, the output fields E_{out1} and E_{out2} represent the results under complex amplitude modulation and phase-only modulation, respectively. (a)-(g) demonstrate the results of convolution for two-dimensional edge detection, directional edges along x, y, 45°, and 135° orientations, x- and $\pi/4$- feature corner detection.

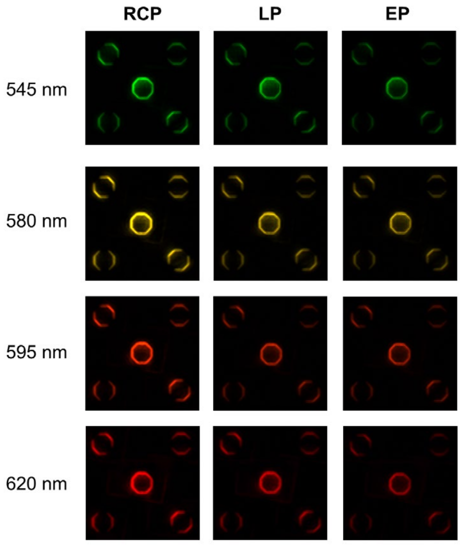

Fig. S7. Experimental results of optical parallel edge detection at different wavelengths and polarization states.

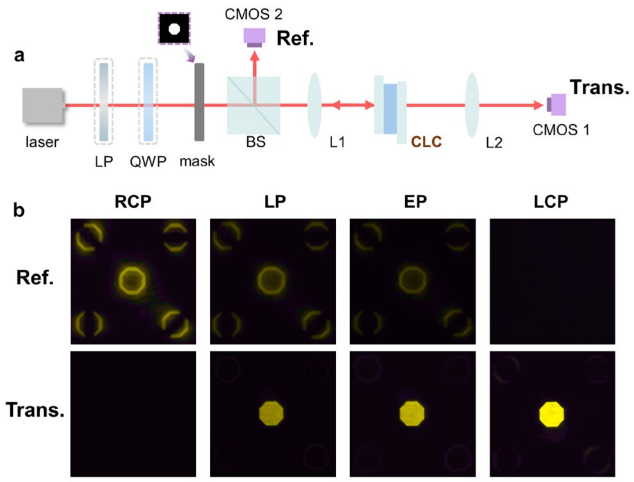

Fig. S8. Dual-mode parallel processing. (a) Optical setup for the simultaneous implementation of the reflective (Ref.) path and transmissive (Trans.) path. (b) The reflective and transmissive experiment results at different polarization state. EP: Elliptical Polarization.

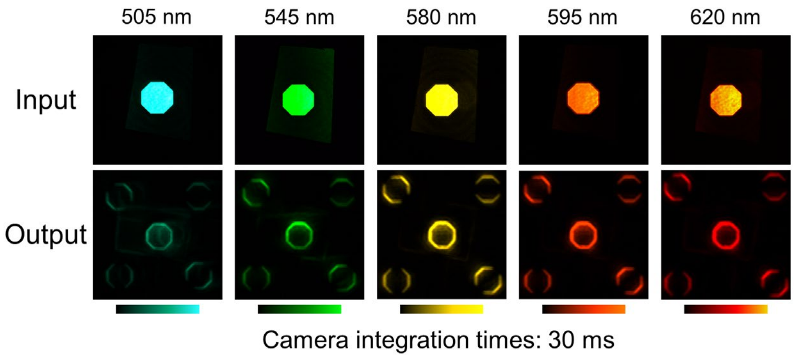

Fig. S9. Comparison of input and output images at different wavelengths under the same camera integration time.

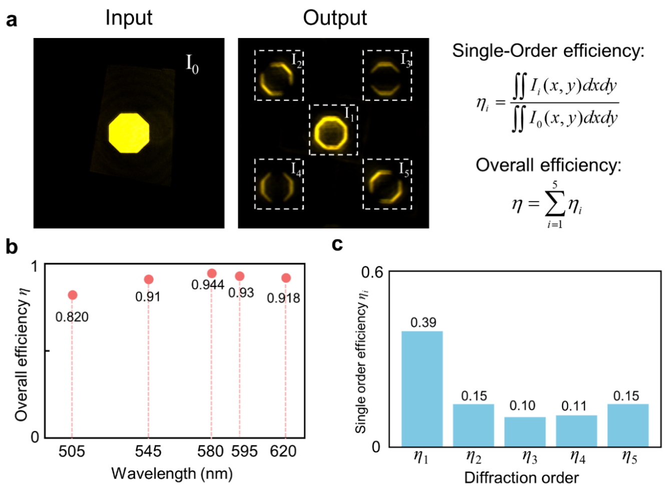

Fig. S10. Quantitative analysis of the intensity efficiency. (a) Schematic of the intensity efficiency measurement (b) Overall intensity efficiency under different wavelength. (c) Average intensity efficiency across multiple diffraction orders.

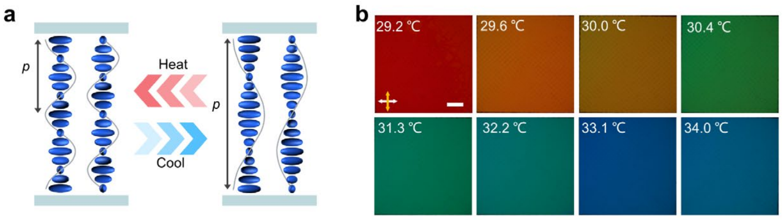

Fig. S11. (a) Schematic of the temperature-dependent CLC helix. (b) Temperature-dependent reflective micrographs of CLC. Scale bar: 250 μm

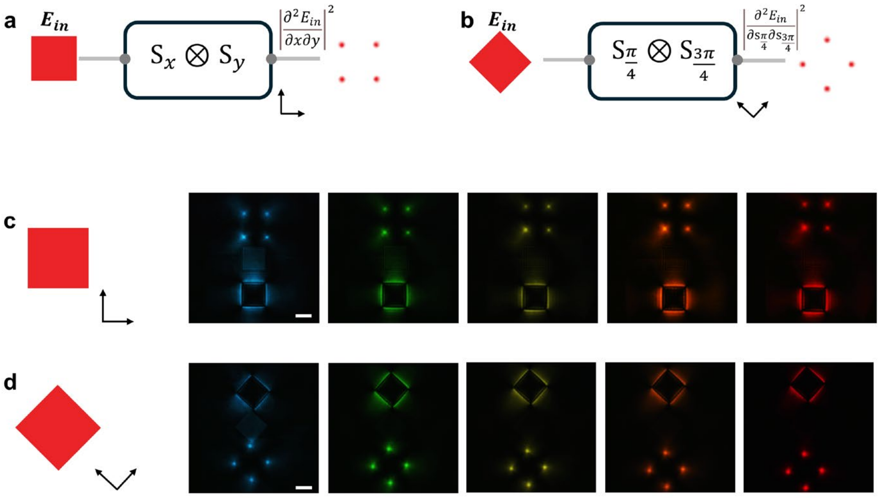

Fig. S12. Parallel optical corner detection. (a) Corner detection mechanism along orthogonal axes: second-order differential $|\partial^2 E_{in}/\partial x\partial y|^2$ applied to input field E_{in} for Cartesian (x-y) orientation analysis. (b) Rotated coordinate corner detection: diagonal (45°/135°) orientation resolved through operator $|\partial^2 E_{in}/\partial s_{\pi/4}\partial s_{3\pi/4}|^2$ where s_θ denotes directional derivative along θ. Parallel corner detection for input light with "square" (c) and "diamond" (d) patterns at 545, 580, 595, and 620 nm. All scale bars are 250μm.

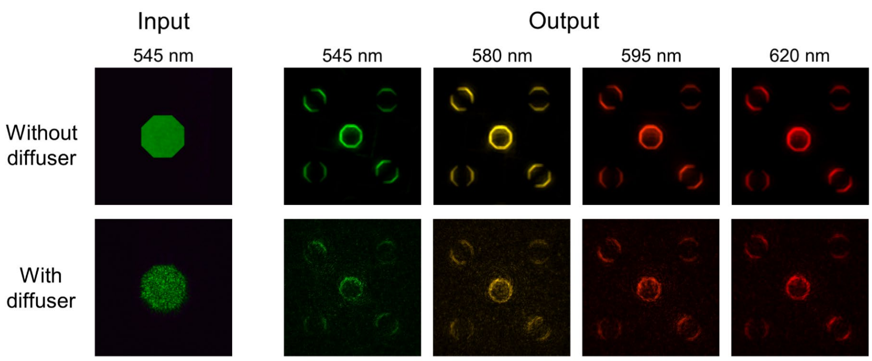

Fig. S13. Comparison between parallel edge detection with and without a diffuser.

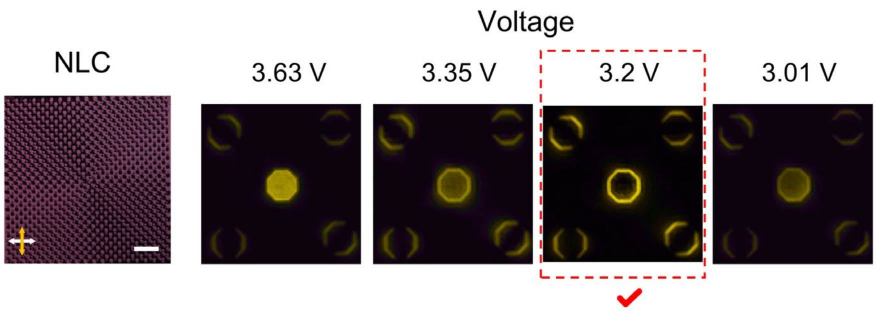

Fig. S14. Parallel image processing under different applied voltages of the NLC.

S_3.

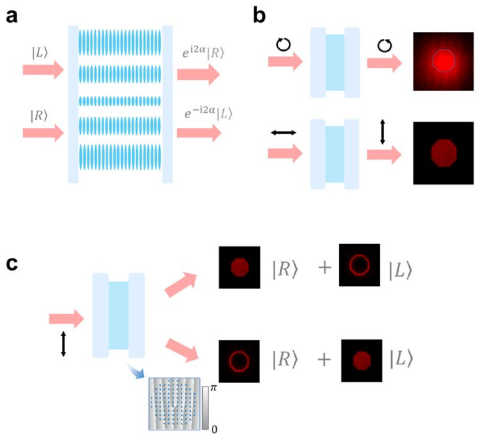

Fig. S15. Polarization-dependent phase modulation by the NLC superstructures. (a) LCP and RCP acquire opposite phase modulation. (b) Generation of amplitude and phase objects by the NLC superstructures. (c) -1st and 1st order diffraction patterns under LP incident light, with insets showing the simulated director orientation angle distributions.

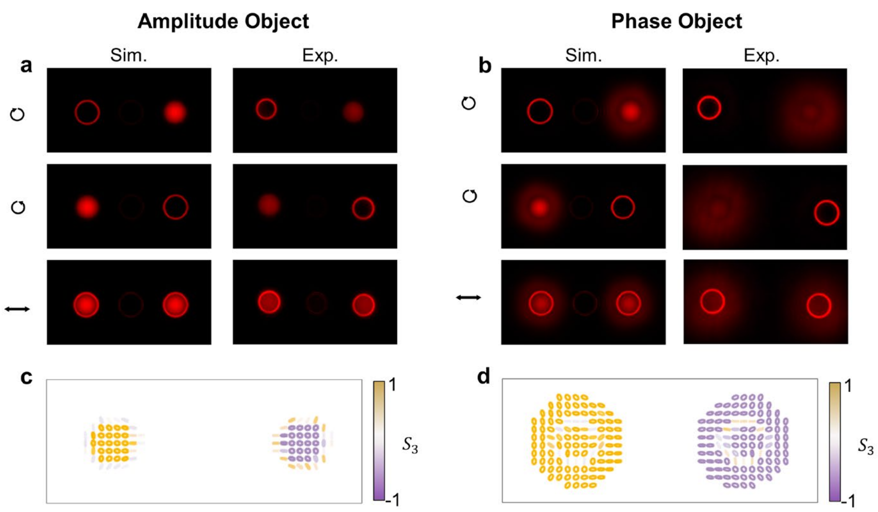

Fig. S16. Optical field characterizations of amplitude and phase object inputs. Simulated and experimental results for amplitude (a) and phase (b) objects under distinct polarization states. Rows corresponds to LCP, RCP and LP light. Polarization maps of output optical beams by amplitude (c) and phase (d) objects. Polarization ellipses are color-coded by Stokes parameter S_3.

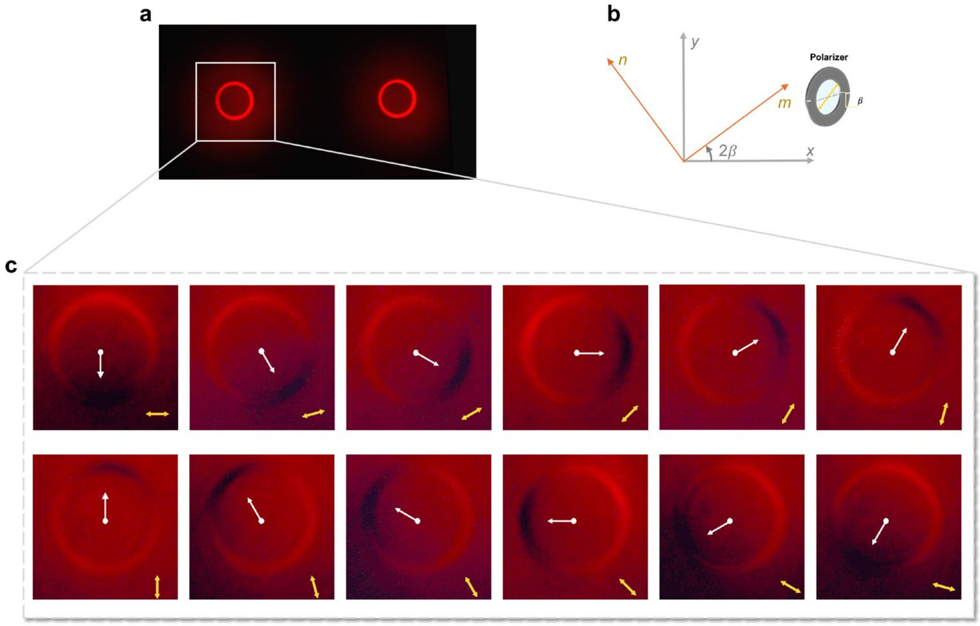

Fig. S17. Polarization-resolved intensity distributions at diverse analyzer angles. (a) Intensity distributions following LP incident light. (b) Coordinate system rotation schematic: the original x-y coordinate system is rotated counterclockwise by 2β to establish the m-n coordinate system, where β corresponds to the analyzer angle. (c) Evolution of light intensity distributions in the -1[st] order diffraction spot [indicated in (a)] with analyzer angles ranging from 0 to 11π/12 (step size: π/12). The yellow double arrow denotes the analyzer orientation, while the white single arrow indicates the azimuthal direction of the intensity minimum within the diffraction spot.

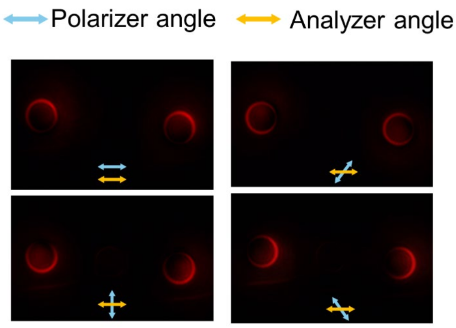

Fig. S18. Experimental results under different polarizer angles.

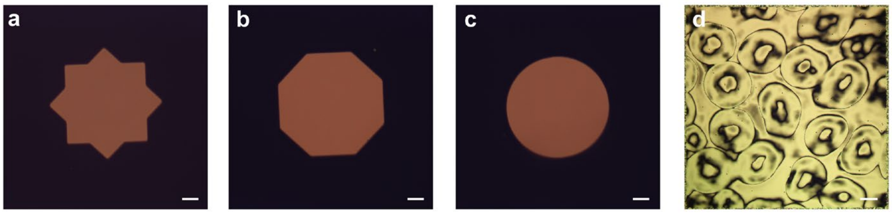

Fig. S19. Micrographs of NLC devices to generate amplitude and phase objects. (a)-(d) correspond to transmission-mode cross-polarized micrographs (scale bar: 250μm) of the NLC samples mentioned in Fig. 3, Fig. 4, Fig. 5(c), and Fig. 5(e), respectively.

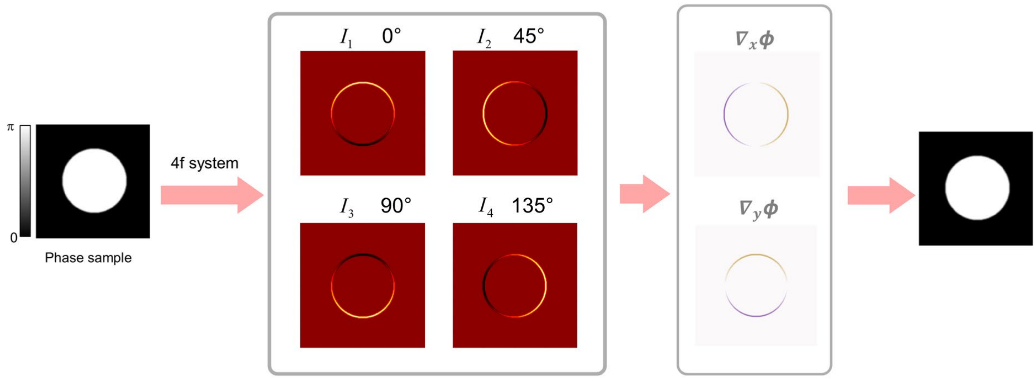

Fig. S20. Phase reconstruction framework. After the phase sample passes through the designed 4f system, the light intensities I_1 to I_4 under the analyzer orientation angles of 0°, 45°, 90°, and 135° are acquired. These intensities are then processed to extract the phase gradient distributions of the phase sample, which are numerically integrated to reconstruct the phase distributions.

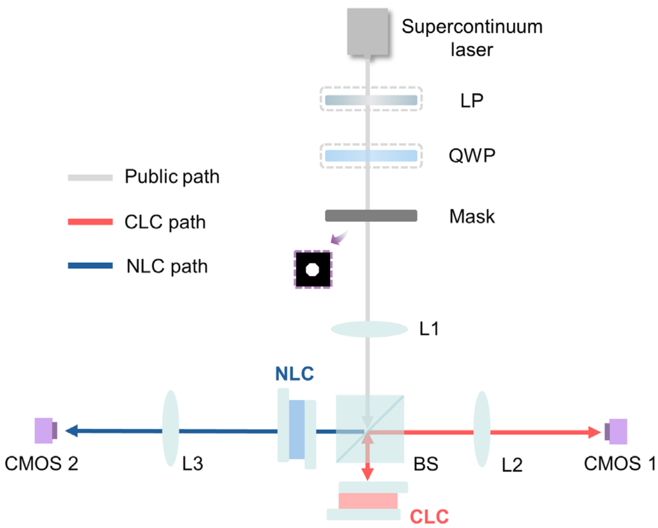

Fig. S21. Schematic of the optical setup for simultaneous CLC- and NLC-based parallel image processing.

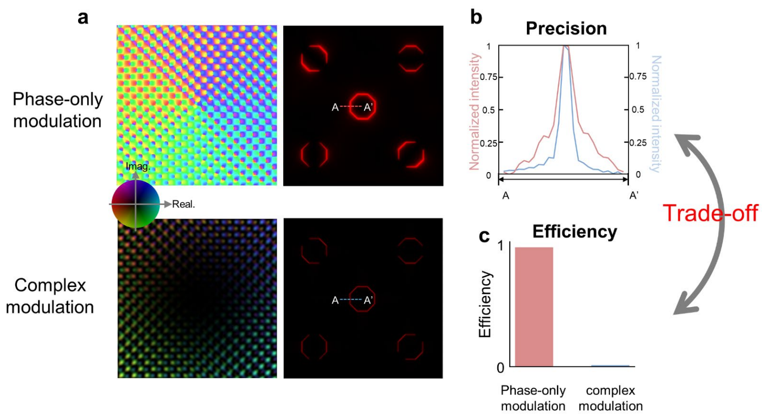

Fig. S22. Schematic of the trade-off between precision and efficiency.

Table S1. Comparison between this work and state-of-the-art optical image processing platforms.

Source	Platform	Parallelism dimensions	Function	Tunability	Efficiency	Operated wavelength
This work	**Photo-patterned LC**	**Spatial, wavelength, polarization**	**Convolution operator, BFI, edges, corners, gradients**	**Yes**	**~ 90%**	**430 ~ 680 nm**
Sci. Adv. (2026)[1]	Metasurfaces	No parallelism	Corners	No	Not reported	450 ~ 638 nm
Optica (2025)[2]	Inverse-designed Metasurfaces	Wavelength, polarization	BFI, edges	No	< 50%	4.37 ~ 4.7 μm
Opt. Lasers Eng. (2025)[3]	SLM	Spatial	BFI, multi-order edges	Yes	Not reported	532 nm
Nat. Nanotechnol. (2024)[4]	Metasurfaces	Spatial, polarization	Arbitrary convolution operator	No	84%	400 ~ 700 nm
Optica (2024)[5]	Thin crystal	Wavelength	Edges	No	< 10%	400 ~ 700 nm
Nat. Commun. (2024)[6]	Metasurfaces	Spatial, wavelength	Multi-order edges	No	< 50%	490 ~ 633 nm
Optica (2023)[7]	Metasurfaces	Polarization	BFI, edges	No	< 10%	1650 nm
ACS Nano (2023)[8]	LC integrated metasurfaces	Polarization	BFI, edges	Yes	30%	450 ~ 633 nm
Nat. Commun. (2022)[9]	Huygens' metasurfaces	No parallelism	Edges, corners, cross-correlation	No	< 50%	3 cm (microwave)
Nat. Photonics (2020)[10]	Cascaded-metasurfaces	Spatial, polarization	Gradients	No	Not reported	1100 ~ 1180 nm
Opt. Lett. (2006)[11]	Phase mask	No parallelism	Edges	No	Not reported	400 ~ 700 nm

* BFI, bright-field imaging; SLM, spatial light modulator

[1] Sci. Adv. **12**, eaed8301(2026)
[2] Optica **12**, 1090 (2025)
[3] Opt. Lasers Eng. **184**, 108669 (2025)
[4] Nat. Nanotechnol. **19**, 471 (2024)
[5] Optica **11**, 1008 (2024)
[6] Nat. Commun. **15**, 9045 (2024)
[7] Optica **10**, 1331 (2023)
[8] ACS Nano **17**, 14678 (2023)
[9] Nat. Commun. **13**, 2188 (2022)
[10] Nat. Photonics **14**, 316 (2020)
[11] Opt. Lett. **31**, 1394 (2006)

Table S2. Comparison of key characteristics among different devices for image processing.

Aspect	Phase mask	SLM	Metasurfaces	Photo-patterned LC	
				CLC	NLC
Principle	Dynamic phase	Dynamic phase	Dynamic phase / geometric phase / resonant / etc.	Spin-selective geometric phase $e^{i2\alpha}\|R\rangle$ or $e^{-i2\alpha}\|L\rangle$	Spin-dependent geometric phase $e^{-i2\alpha}\|R\rangle + e^{i2\alpha}\|L\rangle$
Parallelism dimensions	Spatial	Spatial	Spatial, polarization	Spatial, wavelength, and polarization	
Operated wavelength	Broadband	Narrowband	Broadband	Broad and tunable band	
Tunability	Static	Electric field	Usually static	Electric field, temperature, and photo-rewriting	
Efficiency	High	Moderate	Usually limited	Very high	
Modulation	Binary / few steps	Gray scale	Gray scale	Gray scale	
Operation mode	Trans.	Trans. or ref.	Trans. or ref.	Trans. and ref.	Trans.
Fabrication	Nanofabrication (EBL, FIB, etc.)	CMOS process	Nanofabrication (EBL, FIB, etc.)	Photo-alignment and molecular self-assembly	
UV resistance	High	Moderate	Moderate	Limited	

* Tran., Transmission; Ref., Reflection.

* CMOS, Complementary Metal–Oxide–Semiconductor.

* EBL, Electron Beam Lithography; FIB, Focused Ion Beam.

References

1. J. A. Davis, D. M. Cottrell, J. Campos, *et al.*, "Encoding amplitude information onto phase-only filters," Appl. Opt., **38**, 5004–5013 (1999).
2. J. Chang, V. Sitzmann, X. Dun, *et al.*, "Hybrid optical-electronic convolutional neural networks with optimized diffractive optics for image classification," Sci. Rep. **8**, 12324 (2018).
3. L. Huang, M. Idir, C. Zuo, *et al.*, "Comparison of two-dimensional integration methods for shape reconstruction from gradient data," Optics and Lasers in Engineering **64**, 1–11 (2015).
4. W. H. Southwell, "Wave-front estimation from wave-front slope measurements," J. Opt. Soc. Am. **70**, 998 (1980).
5. C. Kottler, C. David, F. Pfeiffer, *et al.*, "A two-directional approach for grating based differential phase contrast imaging using hard x-rays," Opt. Express **15**, 1175 (2007).